Vortex generator effects on dynamic stall of thick airfoils

Doosttalab, Mehdi; Ferreira, Carlos Simao; Ragni, Daniele; Yu, Wei; Rautmann, Christof

DOI
10.1016/j.renene.2025.123746

Publication date
2025

Document Version
Final published version

Published in
Renewable Energy

Renewable Energy 255 (2025) 123746

Contents lists available at ScienceDirect

Renewable Energy

journal homepage: www.elsevier.com/locate/renene

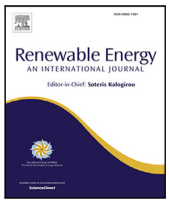

Vortex generator effects on dynamic stall of thick airfoils

Mehdi Doosttalab [a,b,*], Carlos Simao Ferreira [b], Daniele Ragni [b], Wei Yu [b], Christof Rautmann [a]

[a] Nordex Energy SE & Co. KG, Langenhorner Chaussee 600, Hamburg, 22419, Germany
[b] Faculty of Aerospace Engineering, Delft University of Technology, Kluyverweg 1, Delft, 2629 HS, Netherlands

ARTICLE INFO

Keywords:
Wind turbine
Flatback airfoil
Vortex generator
Dynamic stall

ABSTRACT

This study examined the effect of vortex generators on the dynamic stall characteristics of thick wind turbine airfoils with a relative thickness of 35% and trailing edge thickness of 10% and 2%. The experiments were conducted in the TU Delft LTT wind tunnel at a Reynolds number of $Re = 1 \times 10^6$ and dynamic reduced frequency ranging from 0.032 to 0.096. The study investigated the impact of various factors on the dynamic stall characteristics of the airfoils, including the vortex generator's chord position, trailing edge gap, roughness, mean angle of attack, and reduced frequency. The study found that vortex generators delay dynamic stall for thick airfoils by stabilizing the flow during the upstroke phase. However, this can increase the maximum lift overshoot, particularly with flatback airfoils, resulting in a higher drop in lift during dynamic stall. This can potentially increase the dynamic loads on a wind turbine blade due to stall-induced vibrations. The study noted a significant difference in dynamic stall behavior between flatback and non-flatback airfoils. Overall, this research provides valuable insights into the dynamic stall and flow physics characteristics of thick wind turbine airfoils using vortex generators, aiding in more accurate rotor blade design.

1. Introduction

Driven by rising oil prices, increasing energy demand, and environmental concerns, the wind energy industry has experienced rapid growth in recent decades [1]. Over the past three decades, there has been a significant increase in the size of newly developed wind turbines, with rotor diameters expanding from 10–15 m meters to a recent offshore turbine introduced by Vestas measuring 236 m in diameter. Designing and developing such turbines presents a significant challenge for engineers, who balance lightweight and low-cost materials with aerodynamic performance. As a result of the design evolution, modern wind turbines feature longer and more slender rotor blades subjected to significantly higher static and dynamic loads than previous-generation rotors. New design approaches involve increasing the thickness of the inboard-midspan section of the blade, particularly using flatback airfoils. This technique has improved structural and aerodynamic efficiency while reducing blade weight [2]. However, as the rotor blade radius increases, the blade elastic deformations also increase [3], resulting in higher dynamic loads on the turbine. These loads are typically caused by wind gusts, rapid pitch angle changes, yaw angle, wind shear, and aeroelastic torsion due to rotation.

Dynamic flow conditions are usually classified by ranges of reduced frequencies in wind turbines [4]. Reduced frequency is defined as $k = \omega C/2V$. Here V is the airfoil relative velocity, ω is the angular frequency, and C is the chord length. Leishman [5] classified the unsteady flow conditions for rotorcrafts into four categories. Steady flow for $k = 0$. For $0 \leq k \leq 0.05$, the flow is quasi-steady, and the unsteady effects are minor and can be neglected. Unsteady flow can be considered from $k \geq 0.05$, and for $k \geq 0.2$ the flow is categorized as highly unsteady. On the other hand, Pereira et al. [6] suggested considering unsteady effects for $k > 0.02$ for wind energy applications.

Leishman [5] classified the sources of unsteady aerodynamic loading Into two periodic and aperiodic categories. Aperiodic sources of aerodynamic instabilities are wind veer, atmospheric turbulence, wake inductions, and topological rotors for example. On the other hand, yaw misalignment, blade-tower interaction, and wind shear are periodic unsteady aerodynamic sources. As a result of all the previously mentioned phenomena, the blades face different angles of attack through their rotation, which causes different loadings on the blades, thus, different wake development, and different inflow induction.

Dynamic stall results from a rapid change of angle of attack on an airfoil, affecting the boundary layer on the surface of the airfoil so that the onset of stall occurs at several degrees higher than the standard static polar. Furthermore, it delays the flow reattachment process longer than the hysteresis effect, which happens at static lift polar. This phenomenon can lead to high loads on a wind turbine, which can damage or drastically reduce the fatigue life of the turbine.

* Corresponding author at: Nordex Energy SE & Co. KG, Langenhorner Chaussee 600, Hamburg, 22419, Germany.
E-mail address: Mdoosttalab@nordex-online.com (M. Doosttalab).

https://doi.org/10.1016/j.renene.2025.123746
Received 20 September 2024; Received in revised form 10 June 2025; Accepted 10 June 2025
Available online 24 June 2025

Table 1
Dynamic stall boundary conditions for two airfoils of the N117 wind turbine.

Airfoil Thickness			35%			30%	
Wind condition	Wind speed [m/s]	Mean AOA α_m [°]	Amplitude A [°]	Reduced fq k [–]	Mean AOA α_m [°]	Amplitude A [°]	Reduced fq k [–]
NTM	V_{in}+2	10	18	0.16	6	5	0.02
	V_r-2	14	19	0.15	7	5	0.02
	V_r	16	16	0.14	7	6	0.02
	V_r+2	17	17	0.13	5	8	0.02
	V_{out}	18	21	0.09	0	9	0.02
ETM	V_r	17	27	0.14	6	9	0.02
	V_{out}	20	29	0.09	0	10	0.02

A sample of dynamic conditions for two different airfoils of a 117 m diameter Nordex turbine in two different wind turbulence conditions is shown in Table 1. A BEM based in-house load calculation tool, which was developed according to the IEC 61400-1 standard, was used to calculate the dynamic conditions of the airfoils.

The effects of the dynamic flow have been experienced and studied for many years [5]. One of the first researchers who observed this phenomenon is Kramer [7]. He addressed three primary phenomena that caused the delay in the stall onset. The first one is the unsteadiness in the circulation during increasing the angle of attack, which sheds into the wake and reduces the lift. The second relates to the virtual camber in a pitching airfoil, which decreases the leading edge pressure and pressure gradient on the suction side for a given lift coefficient. This effect was also observed by Ericsson [8], Carta [9], Johnson et al. [10], Ericsson et al. [11], McCroskey [12], and Beddoes [13]. The third one is related to the unsteady effects in the boundary layer; especially reversal flows in the presence of external pressure gradients. This has been observed by McAlister et al. [14], Scruggs et al. [15], Telionis [16], and McCroskey [17]. All the mentioned phenomena delay the onset of stall. Ultimately, with a further increase in the angle of attack, a high adverse pressure gradient near the leading edge leads to flow separation. Leishman [5] addressed the formation of a free shear layer downstream of the leading edge, which rolls up quickly and forms vortical structures in the boundary layer that move towards the trailing edge causing a better pressure recovery and an increase in lift. This vortex shedding process has been studied by Ham [18], McCroskey et al. [19], and Beddoes [20]. Later, more experimental studies opened up a better understanding of the onset of dynamic stall by Beddoes in 1978 [21] and 1983 [13], Bobber [22] in 1992, and Chandrasekhar et al. in 1994 [23]. Liiva et al. [24] and Wood [25] performed a full-scale experiment to study the dynamic stall on helicopter rotor. The results showed that the dynamic stall quality is almost Mach number independent under different forcing conditions; however, the quantity behavior of dynamic stall could vary in different Mach numbers, different airfoils, and the presence of 3D conditions [5]. De Tavernier et al. [26] conducted a study on a vertical axis wind turbine airfoil with a maximum thickness of 25.48%. Their findings indicate that the height and mounting position of VGs are crucial factors in delaying or suppressing dynamic stall, depending on the VGs configuration. Mai et al. [27], Heine et al. [28], and Le Pape et al. [29] investigated the impact of leading edge VGs (LEVoGs) on alleviating leading edge vortex shedding during dynamic stall events on rotorcraft airfoils. However, these findings are not applicable to thick airfoils used in wind energy applications, which exhibit no leading edge vortex separation [30] and have different VG geometries, such as circular, backward wedge, and forward wedge. These VGs are installed in close proximity to the leading edge on the pressure side of the airfoil.

Fig. 1 illustrates various stages of dynamic stall, which was calculated using the commercial CFD Fluent solver on an in-house airfoil with 18% relative thickness. The URANS two-equation $k-\omega$ SST turbulence model was utilized, along with the PISO algorithm, to simulate the dynamic stall phenomenon at a Reynolds number of $Re = 6 \times 10^6$. In the first stage, the up-stroke (US-phase), i.e., increasing the angle of attack, on the linear part of the lift curve, the flow reversal appears in the boundary layer due to the reduced adverse pressure gradient caused by the kinematic pitch rate. In the second stage, flow separation occurs at the leading edge, forming a leading edge vortex. If this vortex is moved towards the trailing edge on the suction side, which happens between the stage two and three, it generates additional lift, particularly if it is close to the surface. In some low Mach number cases, it has been reported that this lift overshoot can reach up to 50 to 100% of the maximum static lift coefficient [5]. However, it is important to note that this lift overshoot can result in a sudden nose-down pitching moment, which can be a critical issue from a structural standpoint. This is due to the movement of the suction peak along the suction side of the airfoil, which increases the lever arm length. The speed at which the vortex moves on the airfoil is estimated to be between one-third to half of the free stream velocity [31]. In stage four, beginning of the down-stroke (DS-phase), i.e., decreasing the angle of attack, the vortex leaves the trailing edge and enters the wake downstream of the airfoil. At this point, the flow is fully separated on the suction side of the airfoil, and the flow field is the same as the static flow field at this angle of attack. The vortex shedding of the flow separation on the suction side, causes the lift fluctuations. As the angle of attack decreases, the reattachment process begins, but with a significant delay compared to the static lift polar [32]. This lag is related to the effect of the reverse kinematic-induced camber due to the negative pitch rate on the leading edge pressure gradient. Stage 5 represents a fully attached flow situation. The hysteresis observed in different stages reduces the aerodynamic damping, potentially leading to aeroelastic problems on the rotor blade [5].

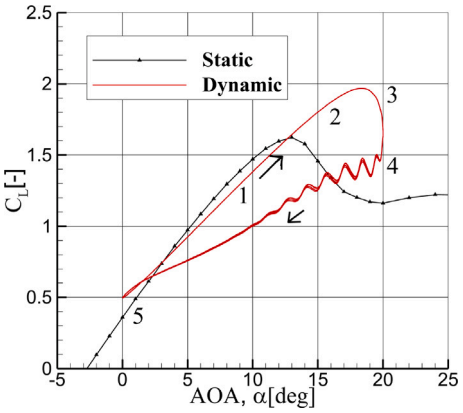

Fig. 1. Different stages of dynamic stall.

As mentioned above, by employing airfoils with high relative thickness towards the mid-span section, they are subjected to increased dynamic loads and fluctuations in high angles of attack. Due to their inherent low stall angle of attack, active or passive flow control methods are necessary to mitigate this issue. Using blunt trailing edge airfoils [2] and/or VGs is one of the most advanced and effective solutions.

These so-called flatback airfoils are generated by adding thickness over the camber line at the aft portion of the sharp railing edge airfoils. Flatback airfoils have several structural and aerodynamic performance advantages compared to the conventional thick wind turbine airfoil with a sharp trailing edge. Due to the reduction of the adverse pressure gradient on the suction side, a flatback airfoil has a higher lift coefficient and higher lift curve slope compared to the sharp trailing edge airfoil with the same thickness [2]. Furthermore, the lift coefficient of flatback airfoils has lower sensitivity to the leading edge soiling than the traditional sharp trailing edge airfoils, which is highly demanded in wind energy. Moreover, because of the increase in the trailing edge gap, these kinds of airfoils have a higher sectional area and sectional moment of inertia for a given airfoil maximum thickness [2]. However, these benefits come with disadvantages, as flatback airfoils are noisier and have a higher drag [33]. The influence of the drag penalty on the rotor's thrust and torque coefficient, as observed in typical inboard twist angles, is not deemed to be severe. In fact, the additional lift generated by a flatback airfoil can effectively compensate for this effect [34].

On the other hand, VGs create vortices in the direction of fluid flow, which are shed near the tip of the vane. These vortices serve to re-energize the boundary layer by promoting mixing between the high-energy fluid outside the boundary layer and the low-energy, low-momentum fluid within the boundary layer, which delay flow separation [35], increase the lift and stall angle of attack. The performance of VGs depends on their size, shape and placement, i.e., mounting chord position on the airfoil [36].

1.1. Objective

As discussed above, several research studies have focused on the dynamic stall and flow physics of thin airfoils [26], but there has been very limited investigation into the implementation of VGs. Accurately assessing loads and designing turbines requires an understanding of the dynamic characteristics of airfoils used in rotor blade design. However, our current knowledge of the dynamic characteristics of thick conventional and flatback airfoils, particularly in combination with VGs, is limited. Insufficient knowledge in this area could lead to significant errors in dynamic load calculations for rotor blades, resulting in poor design and potential damage to wind turbines.

This investigation aims to expand knowledge in this field and explore the effect of VGs on the dynamic stall behavior of high relative thickness wind turbine airfoils. Therefore, a wind tunnel campaign was planned to study the effect of VGs on the dynamic stall characteristics of two thick conventional and flatback wind turbine airfoils. Several VGs chord positions, reduced frequencies and mean angles of attack in different parts of the lift curve, i.e., linear part, pre-stall, stall, and post-stall, were tested for both airfoils in the clean and tripped flow conditions.

2. Experimental setup

The experiments were conducted in the close return low-speed low turbulence wind tunnel (LTT) of the Delft University of Technology [37]. The test section size is 1250 × 1800 × 2600 mm with the nozzle contraction ratio 17.8 : 1, which yields the turbulence intensity of 0.07% at a velocity of 75 m/s. The wind tunnel's maximum speed is 120 m/s at the empty test section. The wind tunnel is powered by a 525 kW variable-speed electric motor, which drives a six-bladed fan. A heat exchanger is installed in the settling chamber to keep the air temperature inside the wind tunnel during the tests constant.

The aerodynamic tests were performed on X-35-02 and X-FB-35-10 airfoils at Reynolds number of $Re = 1.0 \times 10^6$. These airfoils have a maximum thickness of 35%, a leading edge radius of 5%, and trailing edge thickness of 2% and 10%, respectively. Note that the second model is the flatback version of the former model with the same camber and relative thickness position. This flatback airfoil is constructed by adding gradual thickness around the camber line aft of the maximum relative thickness. The models have a chord length of 400 mm and a span of 1248 mm, which result in a blockage ratio of 11% at 30° angle of attack. They were milled from aluminium and mounted vertically in the wind tunnel's test section. The models are instrumented with 90 and 92 pressure taps, respectively. The pressure taps were installed on the model's surface with more density at the leading and trailing edges to resolve the high gradient areas. To simulate the leading edge contamination, trip zig-zag tapes with a thickness of 0.4 mm and width of 12 mm were mounted on the leading edge of the model at 5% and 10% of the chord position on the suction and pressure sides, respectively. The use of zig-zag tape results in a roughness Reynolds number of $R_{kk} = 1 \times 10^3$. Note that due to confidentiality reasons, the exact geometry of the airfoils used in this study cannot be disclosed or published. An approximation of the airfoils is illustrated in Fig. 2.

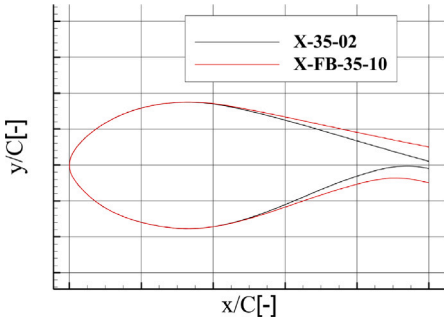

Fig. 2. Approximation of X-35-02 and flatback X-FB-35-10 airfoils geometry.

A series of single-row, plastic injection-molded VGs strips were used on different chord positions on the suction side of the airfoils. These VGs were counter-rotating delta-shaped vanes with a total height of 5 mm, which leads to a roughness Reynolds number of $R_{kk} = 12.5 \times 10^3$. The base plate, which carried the vanes, had a thickness of 1 mm and was affixed to the airfoil surface using a 0.05 mm double-sided tape. The vanes were 12 mm in length and were connected to the base plate at an incidence angle of 18°. The base plate featured rounded leading and trailing edges to prevent flow separation. The vane length, angle, and distance between the centerline of the vane doublets are confidential and cannot be published. The wind tunnel setup and a VGs strip are depicted in Fig. 3.

For static measurements, a turntable was utilized to adjust the angle of attack of the airfoils in the wind tunnel. However, a separate actuator mechanism was employed for dynamic tests. This mechanism was connected to a shaft located at the 1/4 chord of the models and digitally controlled via a servomotor. The setup induced sinusoidal motion on the airfoil, with adjustable mean angle of attack (α_m), amplitude (A), and frequency (fq). The airfoils were pitched at frequencies of 1 Hz, 2 Hz, and 3 Hz, corresponding to reduced frequencies of 0.032, 0.064, and 0.096, respectively. This allowed for testing the airfoils under quasi-unsteady, unsteady, and highly unsteady conditions. The measurement of high pitch frequencies above 3 Hz was not achievable due to the limitations of the setup: including structural vibration of the model, and overheating of the servomotor.

A multichannel pressure data acquisition system was used to measure the static pressure on the surface of the airfoil and calculate the pressure (C_P), lift (C_L), and moment coefficients (C_M). The high-speed pressure scanner employed in this study samples all ports at a frequency of 300 Hz and is averaged for static measurements. Additionally, this sampling rate was utilized for the dynamic measurements, where data was collected for at least 20 cycles.

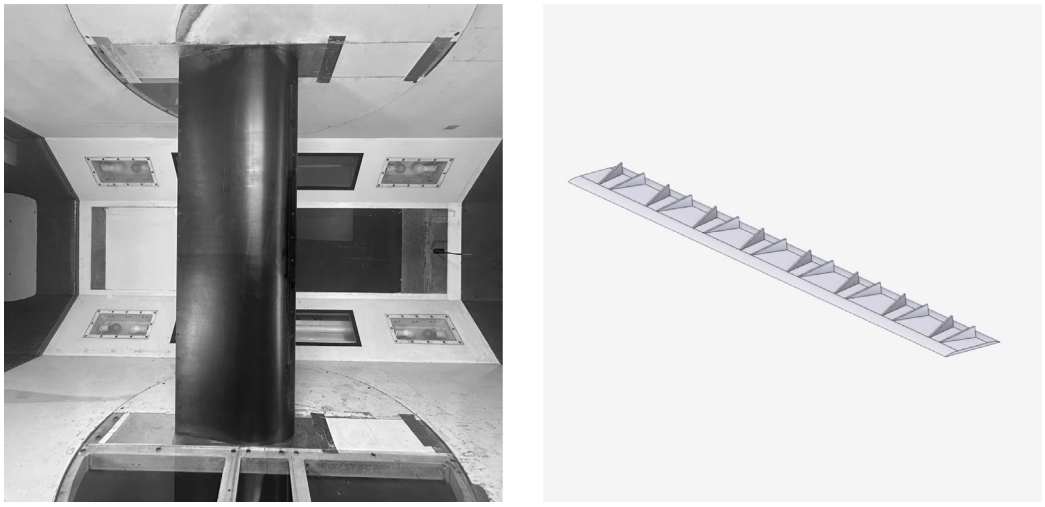

(a) (b)

Fig. 3. Wind tunnel setup and vortex generator strip.

Table 2
Test matrix of both airfoils in the steady conditions.

Airfoil	Reynolds No. [–]	Transition	VG loc. x/C [–]
X-35–02	1.00E+06	Free/Forced	–
X-35–02	1.00E+06	Free/Forced	0.2, 0.3, 0.4
X-FB-35–10	1.00E+06	Free/Forced	–
X-FB-35–10	1.00E+06	Free/Forced	0.2, 0.3, 0.4

A traversed wake rake of 67 total pressure probes located downstream of the airfoil and connected to the data accusation system was used to measure the drag. This method was used only for the X-35-02 airfoil in steady flow conditions. Since the measured drag coefficient using wake rake leads to enormous error for the separated flows [38], the integrated surface pressure measurement method was employed to calculate drag in both static and dynamic conditions, due to the highly turbulent wake at the trailing edge of the X-FB-35-10 airfoil. Moreover, the standard wind tunnel corrections, given by Dalton [39], including the solid and wake blockage and streamline curvature, were applied to the measured data.

Due to the pressure tube length and the fluid characteristics, a method given by Bergh and Tijdeman [40] was used for phase and amplitude corrections of the dynamic pressure measurements, described in Appendix. The corrected data was then used to calculate the aerodynamic coefficients of each airfoil. Finally, the conventional correction methods [39] were used to correct the aerodynamic coefficients. Note the Dalton [39] method is not validated for the unsteady measurements.

A versatile test matrix was prepared to study different static and dynamic conditions on both airfoils, shown in Tables 2 and 3, respectively. 16 static and 192 dynamic measurements were performed on both airfoils. Nevertheless, owing to the constraints of paper size, the current paper does not encompass all of the findings. Note that the mean angle of attack of 6° and 10° were fixed for both airfoils; however, the stall angle of attack of steady measurements was selected as a reference point and two and five degrees before (STL-2°) and after (STL+5°) that were chosen as a mean angle of attack in the near stall conditions respectively. Furthermore, the amplitude of oscillations for pre-stall and post-stall were 10° and 5°, respectively.

3. Results

3.1. Steady conditions

Steady measurements were performed in free and forced transition flow conditions with and without VGs to have reference polars for the dynamic measurements and to see the performance difference between the normal and flatback version of the airfoil. The results are presented in Figs. 4 and 5. Note that the measured drag with VGs shows a periodic wavy pattern, which is due to the presence of the counter vortices of the vanes [36]. The average drag is presented in this study.

Under forced transition conditions, both airfoils exhibit poor aerodynamic performance, especially the X-35-02 airfoil. The stall angle of attack drops from 16° to 5°, and the flow separation on the pressure side starts at a 2° angle of attack. Moreover, a significant flow separation on both sides of the airfoil results in a low lift coefficient between the positive and negative stall angles of attack. These undesirable features are, however, expected due to the high-pressure gradient on both sides of the airfoil, which is a primary motivation for the development of flatback airfoils. It should be emphasized that the flow structure around the airfoils was observed and measured during the steady and dynamic measurements using PIV and the observations are used in this paper to explain and help to understand the dynamic behavior of the flow filed better. More detailed results will be presented in the future publications.

For the X-FB-35-10 airfoil, with only increasing the trailing edge thickness aft of the maximum relative thickness, the lift coefficient was increased again to the free transition level, and the range between the positive and negative stall angles of attack increased rapidly. The drag polars show an increase of the drag in a wide range of angles of attack for the clean condition, compared to the X-35-02 airfoil. However, the drag of the flatback airfoil in forced transition condition is lower than the X-35-02 airfoil in a wide range of angles of attack. This proves that the excessive drag due to the increasing trailing edge thickness is less than the increasing drag caused by separation bubble formation on both sides of the airfoil.

Under forced boundary layer transition conditions, with no VGs, both airfoils show an increased lift after stall with respect to clean conditions. This phenomenon is attributed to the presence of a flow separation bubble, which maintains a constant size between the trailing edge and maximum airfoil thickness on the suction side of the airfoil over a wide range of angles of attack. Furthermore, the pressure and

Table 3
Test matrix of both airfoils in the dynamic conditions.

Airfoil	Reynolds No. [–]	Transition	VG loc. x/C [–]	Mean AOA α_m [°]	Amplitude A [°]	Frequency fq [Hz]	Reduced frequency k [–]
X-35–02	1.0E+06	Free/Forced	–	6°	10°	1, 2, 3	0.032, 0.064, 0.096
X-35–02	1.0E+06	Free/Forced	–	10°	10°	1, 2, 3	0.032, 0.064, 0.096
X-35–02	1.0E+06	Free/Forced	–	STL-2°	10°	1, 2, 3	0.032, 0.064, 0.096
X-35–02	1.0E+06	Free/Forced	–	STL+5°	5°	1, 2, 3	0.032, 0.064, 0.096
X-35–02	1.0E+06	Free/Forced	0.2, 0.3, 0.4	6°	10°	1, 2, 3	0.032, 0.064, 0.096
X-35–02	1.0E+06	Free/Forced	0.2, 0.3, 0.4	10°	10°	1, 2, 3	0.032, 0.064, 0.096
X-35–02	1.0E+06	Free/Forced	0.2, 0.3, 0.4	STL-2°	10°	1, 2, 3	0.032, 0.064, 0.096
X-35–02	1.0E+06	Free/Forced	0.2, 0.3, 0.4	STL+5°	5°	1, 2, 3	0.032, 0.064, 0.096
X-FB-35–10	1.0E+06	Free/Forced	–	6°	10°	1, 2, 3	0.032, 0.064, 0.096
X-FB-35–10	1.0E+06	Free/Forced	–	10°	10°	1, 2, 3	0.032, 0.064, 0.096
X-FB-35–10	1.0E+06	Free/Forced	–	STL-2°	10°	1, 2, 3	0.032, 0.064, 0.096
X-FB-35–10	1.0E+06	Free/Forced	–	STL+5°	5°	1, 2, 3	0.032, 0.064, 0.096
X-FB-35–10	1.0E+06	Free/Forced	0.2, 0.3, 0.4	6°	10°	1, 2, 3	0.032, 0.064, 0.096
X-FB-35–10	1.0E+06	Free/Forced	0.2, 0.3, 0.4	10°	10°	1, 2, 3	0.032, 0.064, 0.096
X-FB-35–10	1.0E+06	Free/Forced	0.2, 0.3, 0.4	STL-2°	10°	1, 2, 3	0.032, 0.064, 0.096
X-FB-35–10	1.0E+06	Free/Forced	0.2, 0.3, 0.4	STL+5°	5°	1, 2, 3	0.032, 0.064, 0.096

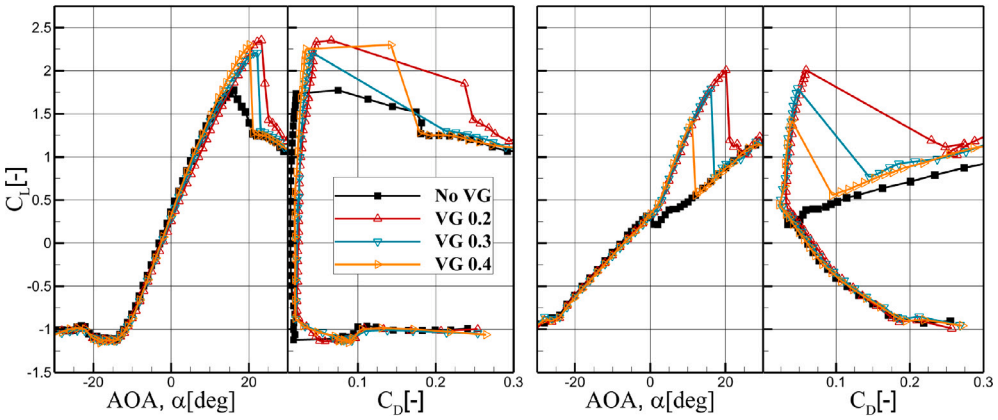

Fig. 4. Steady polar curves for X-35-02 airfoil with VGs [$Re = 1 \times 10^6$, Left: Free transition, Right: Forced transition].

flow stability increase with increasing angle of attack on the pressure side of the airfoil. The back camber on the pressure side near the trailing edge acts like a flap and is more effective at higher angles of attack, further contributing to the lift increase in post-stall angles. However, the lift eventually decays as the separation bubble on the suction side bursts towards the leading edge, which is not depicted in this illustration.

The figures provide an overview of the airfoils performance at various chord positions of the VGs. The results in free transition indicate that moving the VGs towards the leading edge leads to an increase in the stall angle of attack, a slight decrease in the lift curve slope, and an increase in drag. These behaviors can be attributed to the size of the vortices generated above the surface of the airfoil. Positioning the VGs further downstream will restrict the amount of high-energy flow the vanes can direct into the boundary layer, as the thickness of the boundary layer increases. Consequently, weaker vortices are generated above the airfoil, making it more prone to flow separation in adverse pressure gradients. The increase in drag is attributed to the earlier transition of the flow to a turbulent state. On the other hand, a substantial performance gain can be seen using the VG in forced transition conditions. The lift coefficient and stall angle of attack are significantly increased and the sensitivity of the airfoil to the leading edge roughness is decreased, for the X-35-02 airfoil compared to the no-VGs configuration. Generally, a similar trend is observed for the X-FB-35-10 flatback airfoil. However, one difference for the flatback airfoil is that the stall angle of attack is higher for a certain VGs chord position in forced transition condition compared to the X-35-02 airfoil, which is due to a lower pressure gradient on the suction side of the airfoil. Furthermore, a more abrupt stall characteristic is observed by moving the VGs towards the leading edge in both free and forced transition flow regimes. This can potentially lead to wind turbine instability and should be considered during the turbine design. Note that the drag of the flatback airfoil is hardly affected by the VGs in both free and forced transition flow, which is due to the high form drag of the airfoil.

Fig. 6 presents the surface flow visualization of the X-35-02 airfoil at two different angles of attack and $Re = 1 \times 10^6$ in forced transition. The leading edge is on the left, and the trailing edge is on the right side of the pictures. In the absence of VGs, flow separation is already evident at the trailing edge even for $\alpha = 3°$. However, installing VGs allows the flow to remain attached to the airfoil surface, even at higher angles of attack of 8 degrees. Downstream of the VGs, the surface streamlines of the vortices are visible. It should be noted that these images depict the mid-span of the model, and the surface paint run near the trailing edge is a result of gravity and lack of flow momentum, rather than any interaction between the model and the wind tunnel wall.

Fig. 7 shows the pressure coefficient comparison for X-35-02 and X-FB-35-10 airfoils in free and forced transition flow regimes with the VGs at 30% of the chord length at the angles of attack of 4, 15, and 22 degrees. Note that the pressure discontinuity in free transition flow regimes is related to forming the laminar separation bubble, and the effects of the VGs and zig-zag tape are visible as a pressure leap.

Both airfoils show similar performance in free transition flow regime. Due to the high-pressure gradients on the surface of the airfoils, the flow undergoes turbulent transition just after the onset of the laminar separation bubble. The transition point moves towards the leading edge, with increasing the angle of attack. At low angles of attack, the flow remains attached to the surface of airfoils; however,

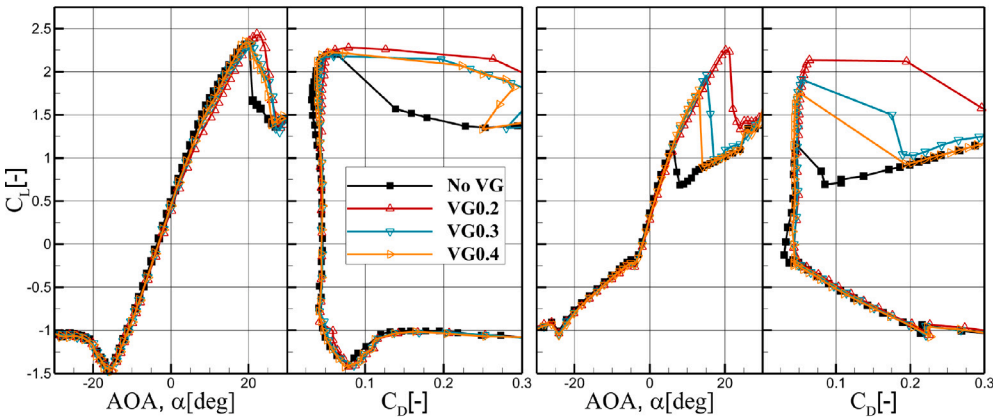

Fig. 5. Steady polar curves for X-FB-35-10 airfoil with VGs [$Re = 1 \times 10^6$, Left: Free transition, Right: Forced transition].

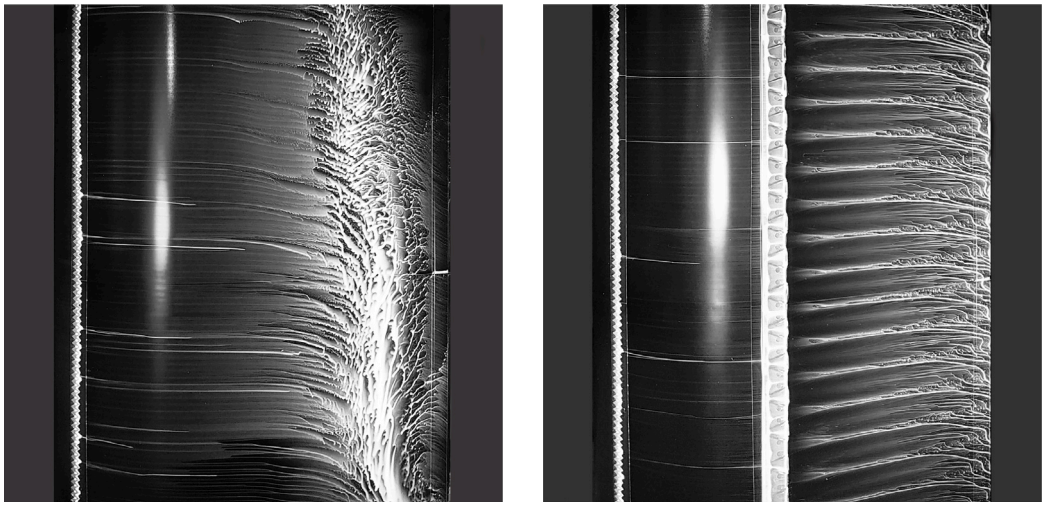

(a) $\alpha = 3°$, No-VGs (b) $\alpha = 8°$, VGs at x/C=40%

Fig. 6. Surface flow visualization on the suction side of the X-35-02 airfoil, in forced transition condition [$Re = 1 \times 10^6$].

with increasing the angle of attack to 15°, the trailing edge separation forms at the end part of the suction side of the X-35-02 airfoil, but it is not extended enough to stall the airfoil. The lower pressure gradient of the X-FB-35-10 airfoil on its suction side is visible at $\alpha_m = 15°$. With further increasing the angle of attack, trailing edge flow separation forms on both airfoils, which causes the stall.

In forced transition flow regime, the X-35-02 airfoil shows flow separation on the suction side at $\alpha_m = 4°$, which progressively enlarges with increasing the angle of attack. The X-FB-35-10 airfoil, on the other hand, shows no sign of flow separation at $\alpha_m = 4°$. As expected, the flow separation size on the suction side of both airfoils increases with increasing angle of attack. Notice the big difference between the maximum suction peaks at high angles of attack between free and forced transition flow regimes. The X-FB-35-10 airfoil exhibits slightly higher suction peaks in both free and forced transition flow regimes because of the lower pressure gradient aft of the maximum relative thickness.

Implementing VGs on the X-35-02 airfoil eliminates the flow separation and the associated aft pressure plateau. Notably, the flow remains attached up to an angle of attack of 22°, despite the presence of high pressure gradients. This behavior is responsible for the abrupt stall characteristics observed. Due to the lower pressure gradient of the flatback airfoil, the pressure distribution remains comparable to that of the free transition regime at angles of attack of 4° and 15°. At an angle of attack of 22°, a minor flow separation region is observed at the trailing edge. This flow separation region expands at a slower rate than that of the X-35-02 airfoil, resulting in smoother stall characteristics. Overall, the outcomes observed under steady conditions using VGs exhibit minimal deviation from prior investigations conducted on thinner airfoils by Timmer et al. [36] and Baldacchino et al. [41].

3.2. Unsteady conditions

Fig. 8 presents the dynamic normal coefficient polars of X-35-02 and X-FB-35-10 airfoils with and without VGs in different mean angles of attack and reduced frequency of $k = 0.064$ in free and forced transition flow regimes. Note that the DS-phases are depicted with dash-dot-dot lines. During the dynamic loops, if the flow remains attached to both airfoil surfaces, the standard deviation of the normal force coefficients in the US and/or DS-phase is low. On the other hand, when a separation bubble is present on one or both sides of the airfoil, its unsteady behavior is seen in the standard deviation of the dynamic C_N values. Note the oval dynamic cycles below the steady stall are counterclockwise i.e., the US-phase is on the lower and the DS-phase is on the upper side of the loop, respectively.

In free transition flow and no-VGs configuration at $\alpha_m = 10°$, both airfoils exhibit the same trend in the US-phase i.e., the lower part of the loops. The C_N is lower than the static force due to the pressure adaptation lag of the flow to the new increasing angle of attack. The C_N and the normal force range (NFR) are higher for the X-FB-35-10 airfoil

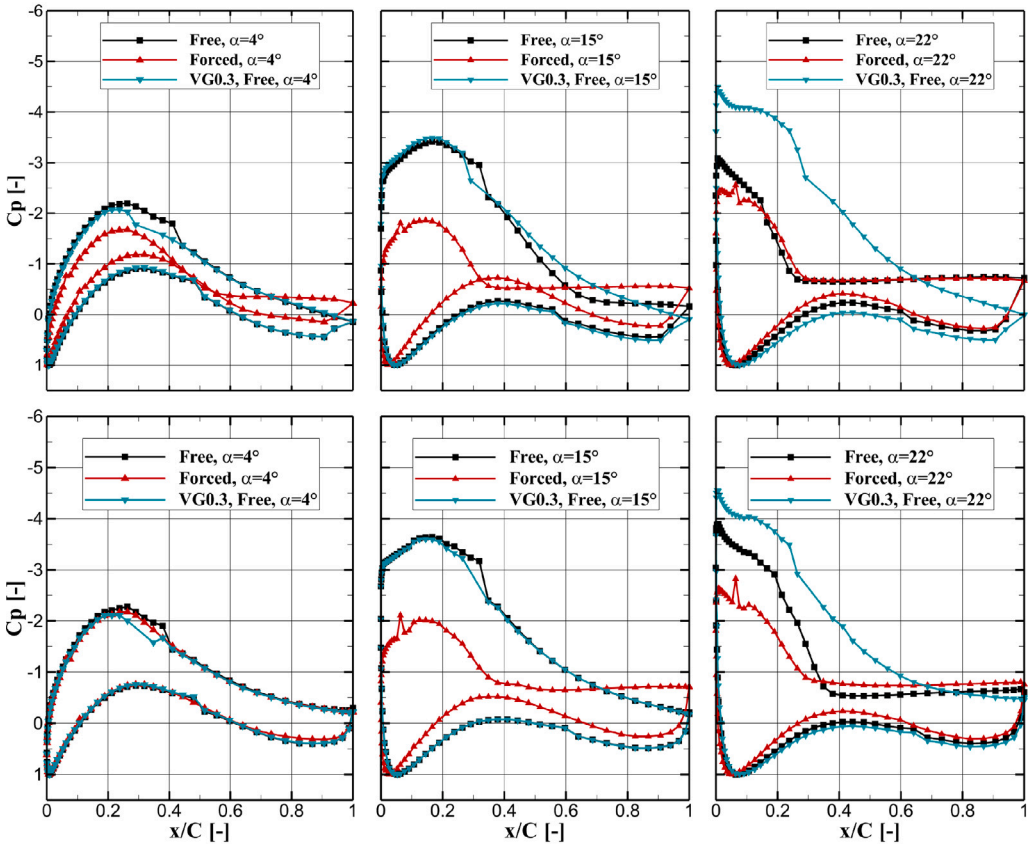

Fig. 7. Pressure coefficient distribution comparison in free and forced transition flow regimes, with VG at x/C = 0.3 [$Re = 1 \times 10^6$, Top: X-35-02, Bottom: X-FB-35-10].

than for the X-35-02 airfoil, due to better pressure gradient conditions above the airfoil. As the airfoils approach the top stagnation angle (TSA), trailing edge separation forms on the suction side. For the X-35-02 airfoil the TSA is beyond the steady stall angle of attack, and the pressure gradient on the suction side of the airfoil is such that the trailing edge separation bubble bursts towards the leading edge and the C_N drops, and the airfoil stalls dynamically. Note that the separation bubble becomes smaller and disappears with a decrease in the angle of attack. This can be detected by decreasing the standard deviation of the C_N at the end of the DS-phase. Thus, the dynamic C_N slope remains low in a large portion of the DS-phase. Before the bottom stagnation angle (BSA), the flow is again fully attached and the dynamic C_N approaches the static value, due to decreasing the pitching rate ($d\alpha/dt$) and pressure adaptation lag close to the BSA. The US-phase begins again in fully attached condition, and the C_N remains below the static values as described before. Consequently, the dynamic loops are eight-shaped. However, for the X-FB-35-10 airfoil, the TSA equals the steady stall angle of attack. Due to the lower pressure gradients, the separation bubble near the trailing edge expands partially above the airfoil. Still, it is not extended enough to fully stall the airfoil; however, a slight decrease of the C_N is visible at the TSA. For this reason, the standard deviation of the dynamic C_N increases at the beginning of the DS-phase. In the attached flow part of the DS-phase, the C_N is higher than the stationary polar because of the flow pattern adaptation lag. With the further decrease of the angle of attack, the separation bubble becomes smaller and eventually disappears before the BSA, leading to stable flow. Hence, the standard deviation of C_N decreases. Compared to the X-35-02 airfoil, these favorable conditions increase the flatback airfoil's mean dynamic normal slope (MDNS). MDNS is defined as a line, which connects the C_N of the BSA to the TSA. By increasing the mean angle of attack to $\alpha_m = STL\text{-}2°$ for the same flow and airfoil configurations, both airfoils exhibit the same eight-shape dynamic C_N loops, as a result of the onset of dynamic stall. The X-FB-35-10 airfoil exhibits a longer C_N US-phase than the other airfoil due to its more stable flow characteristics. However, the flatback airfoil has a more abrupt stall characteristic than the X-35-02 airfoil. A higher stall angle of attack generates higher pressure gradients on the suction side of the airfoil, which leads to a faster expansion of the separation bubble, compared to the X-35-02 airfoil. Furthermore, the lowest C_N of this case in the post-dynamic stall is even lower than the end of the DS-phase, and the NFR value remains higher for the flatback airfoil. The X-35-02 airfoil exhibits a slightly higher MDNS than the flatback airfoil.

In the absence of VGs and under free transition flow regime, the post-stall mean angle of attack (i.e., $\alpha_m = STL{+}5°$) results in oval-shaped dynamic loops that cycle clockwise, in contrast to the linear part. The X-35-02 airfoil exhibits a smooth, steady stall compared to the abrupt stall of the flatback airfoil, which results from the gradual movement of the trailing edge separation towards the leading edge during the stall. Thus, the trailing edge separation bubble of the X-35-02 airfoil is smaller than the flatback airfoil at the BSA, leading to an increase in normal force compared to the flatback airfoil. On the other hand, the X-FB-35-10 airfoil displays a larger separation bubble at the BSA compared to the X-35-02 airfoil. Under deep stall conditions, the trailing edge vortex of the flatback airfoil combines with the suction side separation bubble, creating a multiple separation bubble zone that is not efficiently affected by increasing the angle of attack. Therefore, the dynamic C_N increases less than that of the X-35-02 airfoil during the US-phase, resulting in a lower NFR value than the X-35-02 airfoil. During the DS-phase, the large separation bubble remains longer on the airfoil due to the pressure lag, causing the dynamic C_N to drop below the static C_N. Since the separation bubble on the X-35-02 airfoil retracts faster than that of the flatback airfoil, the dynamic C_N increases from the one quarter of the DS-phase.

Under forced transition flow and in the absence of VGs, the dynamic cycles for the X-35-02 airfoil differ from those of the flatback airfoil.

Due to the heavy flow separation on both sides of the airfoil at the end of the US and DS-phases, the C_N cycles remain flat for different mean angles of attack. The TSA and BSA are beyond the positive and/or negative stall angles of attack and the MDNS is close to the C_N of the static curve. However, the X-FB-35-10 airfoil shows a different behavior. At $\alpha_m = 10°$ and $\alpha_m = STL - 2°$, the dynamic stall occurs at both mean angles of attack. This is because the BSA is in the linear stable part of the steady polar, and the US-phase starts with an attached flow on the suction side of the airfoil. The flow starts to separate before the TSA, where the deviation of the dynamic C_N becomes visible and remains separated until just before the BSA. It should be noted that during the DS-phase, the C_N follows the slope of the post-stall steady C_N. Once again, the MDNS of the flatback airfoil remains higher than the other airfoil. Therefore, the C_N overshoot values are much higher than those of the X-35-02 airfoil in forced transition conditions. At $\alpha = STL + 5°$, due to a large separation bubble above the airfoil, both airfoils exhibit flat clockwise dynamic cycles around the steady polar.

In free transition flow with VG at 30% of the chord length, both airfoils show the same characteristics at $\alpha_m = 10°$. In the US-phase, the flow remains attached up to the TSA, and the C_N remains below the steady polar due to the pressure adaptation lag. As the airfoils approach the TSA and the pitching rate decreases, flow separation forms above both airfoils near the trailing edge. The separation becomes smaller with decreasing the angle of attack during the DS-phase and disappears at around $2/3$ of the DS-phase. Note that the dynamic C_N remains above the steady polar again due to the pressure adaptation lag. The flatback airfoil exhibits more flow instabilities at TSA, because of the lower distance to the steady stall angle of attack and the trailing edge vortex. Comparing these results with the no-VGs configuration shows that the US and DS-phases C_N slopes, MDNS, and NFR increase when using VGs for both airfoils. Moreover, the difference between the dynamic cycles of both airfoils is reduced since the X-35-02 cycle transforms into an oval shape.

The free transition flow regime results with VG at $\alpha_m = STL\text{-}2°$ show eight-shaped dynamic cycles for both airfoils. Using VGs reduces the difference between the steady polars of the airfoils, resulting in similar dynamic cycle characteristics. However, the standard deviation of the US-phase of the flatback airfoil is higher than that of the X-35-02 airfoil due to the trailing edge vortex and the trailing edge separation forming before the TSA. In both cases, the C_N drops below the value of the BSA. Note that the separation bubble remains above the airfoil, and the flow recovery occurs at the BSA in the US-phase. Furthermore, the standard deviation of the DS-phase of the flatback airfoil is higher than that of the X-35-02 airfoil due to the combination of different vortex systems, including the trailing edge vortex, suction side separation bubble, and the VGs remaining vortices. Moreover, the NFR is increased for both airfoils when using VGs compared to the no-VGs configuration.

By increasing the mean angle of attack to $\alpha_m = STL{+}5°$ for the same flow and airfoil configuration, both airfoils exhibit clockwise dynamic cycles. However, due to its smooth stall characteristics, the flatback airfoil has a higher NFR than the X-35-02 airfoil. Flow attachment is partially recovered as the BSA is approached at the end of the DS-phase. Due to the unstable flow conditions, different separation bubble sizes can be formed at the BSA at each cycle, which will be developed differently above the airfoil during the US-phase, resulting in bifurcation flow above the airfoil. Compared to the no-VGs configuration, the NFR increases for the flatback airfoil and decreases for the X-35-02 airfoil. Moreover, the MDNS increases for the X-35-02 airfoil and decreases for the flatback airfoil. The results show that if the BSA approaches the steady stall angle of attack, a reduction in the separation bubble size leads to a slight increase in the dynamic C_N in the US-phase.

The results obtained from the forced transition flow and VGs configuration at $\alpha_m = 10°$ show dynamic stall cycles for both airfoils. The US-phase for both airfoils begins in an attached flow condition and remains attached up to the TSA. However, the dynamic stall is not abrupt for both airfoils. Furthermore, the bifurcation flow is visible at the DS-phase. For the flatback airfoil the flow recovery in some cycles is fast and the dynamic C_N moves above the steady polar at the begening of the DS-phase. The trailing edge flow separation occurs at the beginning of the DS-phase and is trapped downstream of the VGs, and cannot expand fully above the airfoil. Thus, the dynamic stall is smooth. At the end of the DS-phase, the flow starts to reattach, increasing the C_N before the BSA.

At $\alpha_m = STL\text{-}2°$ in forced transition flow regime with VGs configuration, both airfoils exhibit dynamic stall occurrence. However, unlike the free transition cases, the dynamic C_N drops gradually for both airfoils. This is due to the lower stall angle of attack, i.e., lower maximum lift and pressure gradient above the airfoils at TSA in forced transition conditions, compared to the free transition cases. On both airfoils, the flow starts to detach before the TSA. The NFR and MDNS are higher for these cases compared to the free transition flow. At post-stall, i.e., $\alpha_m = STL{+}5°$, the clockwise dynamic cycles remain very close to the steady polars due to a large separation bubble above the airfoils. A small bifurcation flow effect can be observed for both airfoils.

Figs. 9, 10, and 11 present the pressure coefficient distributions of the three cases, from the above polars at three different angles of attack (1/4, 1/2, and 3/4 of the US and DS-phases). Fig. 9 displays both airfoils' steady and dynamic pressure distributions at a mean angle of attack of 10° in free transition flow and without VGs configuration. At an angle of attack of 5°, there is no indication of flow separation at the trailing edge during the US-phase for both airfoils. The suction peak is lower than the static pressure distribution due to the pressure adaptation lag and reduction of relative velocity above the surface caused by the pitching of the airfoil. If the flow remains attached, the suction peak pressure reduction is also visible in the other US-phase figures.

When observing the US-phases for the X-FB-35-10 airfoil, the suction peak pressure slowly increases with an increase in the angle of attack. The dynamic movement of the airfoil alters the flow regime and eliminates the laminar separation bubble. Conversely, during the DS-phase, the maximum suction peak is higher than the static peak for the attached flow part of the stroke. This explains the higher normal lift at that section of the stroke. Additionally, the laminar separation bubble is visible again on the suction side, aft of the suction peak at the end of the DS-phase, but it is shifted towards the leading edge.

However, for the X-35-02 airfoil the TSA exceeds the static stall angle of attack and the lift drop in the dynamic stall is higher than the flatback airfoil. As expected, the suction peak during the US-phase is lower than the static pressure coefficient. The pressure coefficient near the trailing edge on the suction side is the same as the static measurement and even falls below the static curve at the upper part of the US-phase, resulting in a higher pressure gradient. Flow separation is visible on the suction side in the DS-phase as a flat plateau before the trailing edge. This separation bubble becomes smaller as the angle of attack decreases. Additionally, the suction peak, forms as a plateau near the leading edge, becomes curved and moves towards the trailing edge.

The steady and dynamic pressure distributions of both airfoils with VGs at a mean angle of attack of 10° in forced transition flow are presented in Fig. 10. During the US-phase, the flow remains attached for both airfoils, and the same behavior is observed as described above. However, flow separation on the pressure side of the X-35-02 airfoil is observed at low part of the US-phase due to a high pressure gradient and thick, turbulent boundary layer. This separation results in a decrease in lift, which is eliminated at higher angles of attack. As previously described, due to the angle of attack stagnation at the end of the US-phase from one side and a very high pressure gradient on the other side, the flow separation moves from the trailing edge towards the leading edge of both airfoils. However, it remains downstream of the VGs, which is visible as a flat pressure plateau extended from the trailing edge to the VGs position during the DS-phase. The suction peak remains high upstream of the VGs during the DS-phase. Note the higher

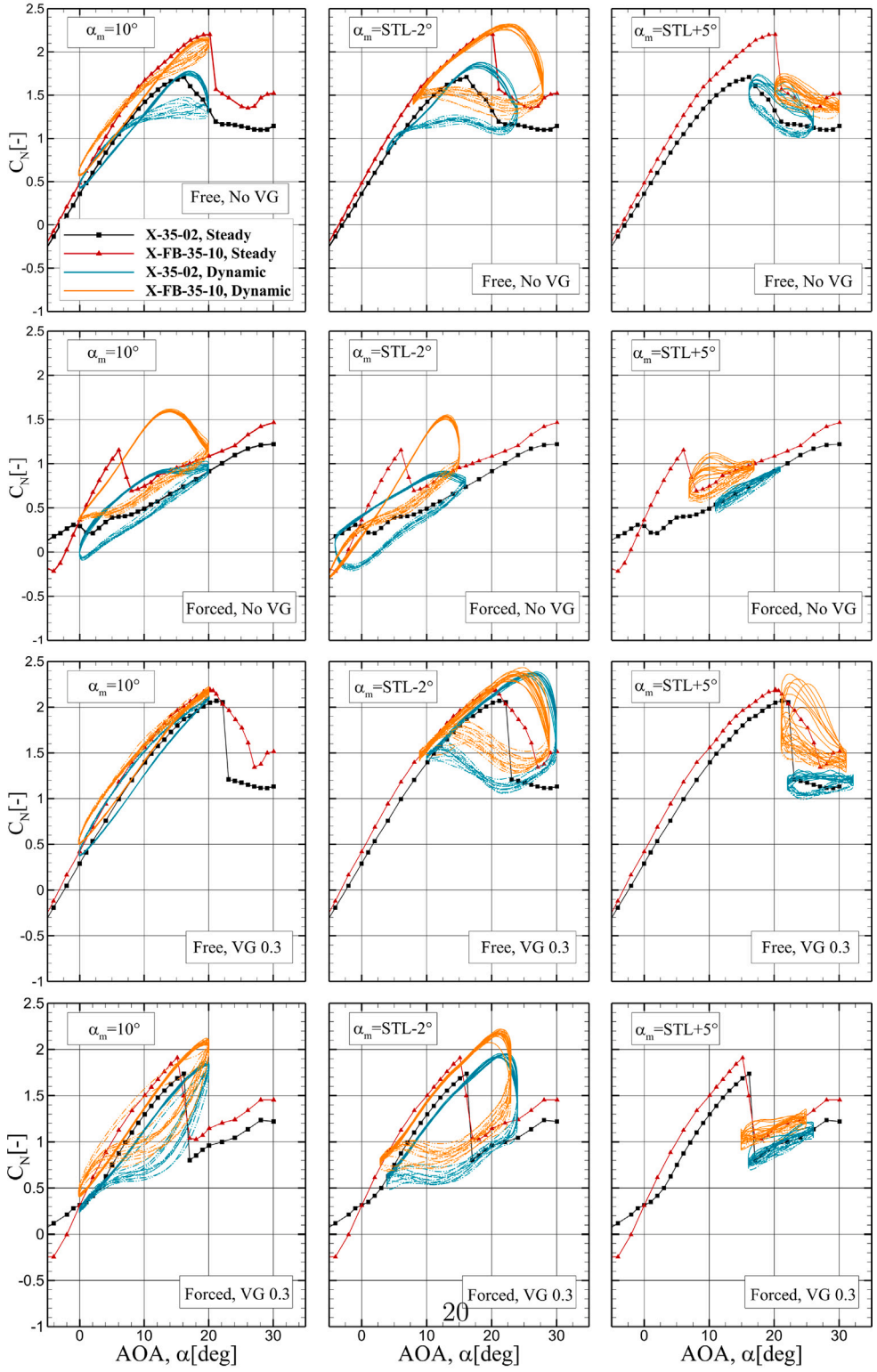

Fig. 8. Comparison between the static and dynamic normal force coefficients in clean and with VGs configurations for X-35-02 and X-FB-35-10 airfoils [$k = 0.064$, $Re = 1 \times 10^6$].

suction peak of the flatback airfoil during the DS-phase compared to the other airfoil.

At the mean angle of attack of $\alpha_m = STL\text{-}2°$ in free transition flow with VGs configuration, the suction peak increases during the US-phase, moves towards the leading edge, as the angle of attack increases, as illustrated in Fig. 11. Both airfoils form a suction pressure plateau, but despite the very high-pressure gradient at the end of the US-phase, no trailing edge separation is observed. Note that the pressure gradient aft of the VGs, and the suction peak of the X-35-02 airfoil is slightly higher than that of the flatback airfoil at the end of the US-phase. Due to a very high-pressure gradient on the suction side at the TSA, the separation bubble expands rapidly from the trailing edge towards the leading edge of both airfoils. The separation bubble expands upstream of the VGs at the beginning of the DS-phase, and the effects of the VGs

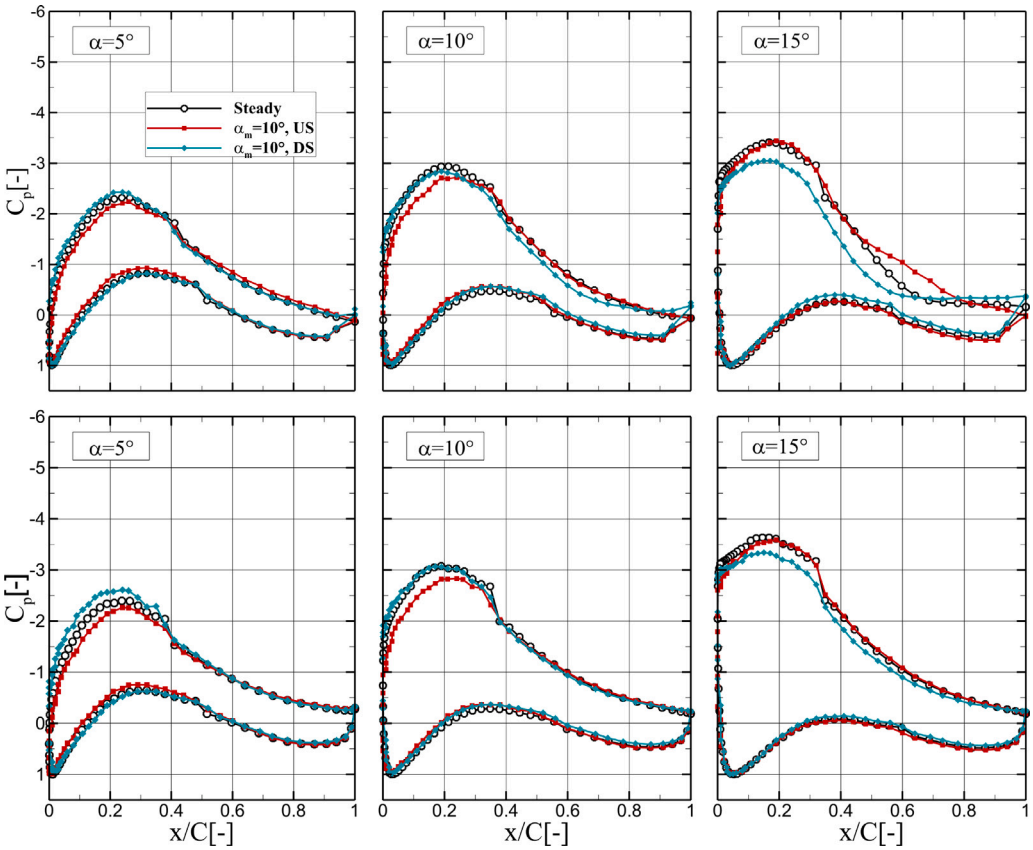

Fig. 9. Steady and dynamic Pressure coefficient distribution comparison in free transition flow regime [$Re = 1 \times 10^6$, $k = 0.064$, $\alpha_m = 10°$, No-VGs, Top: X-35-02, Bottom: X-FB-35-10].

are visible in the pressure distribution as the flow starts to reattach to the surface of the airfoils at the end of the DS-phase. It should be emphasized that the flow reattachment process in the DS-phase for the flatback airfoil is faster than that of the X-35-02 airfoil due to its lower pressure gradient on the suction side.

Fig. 12 shows the effect of the reduced frequency on the dynamic normal coefficient characteristics of both airfoils with no-VGs configuration in free and force transition flow regimes. At $\alpha_m = 10°$ and in free transition flow, the pressure adaptation lag for the X-35-02 airfoil increases with increasing reduced frequency. This leads to a reduction in C_N during the US-phase. Additionally, the trailing edge separation occurs at higher angles of attack with increasing reduced frequency, and the maximum C_N occurs at higher angles of attack. These phenomena alter the shape of the DS-phase. It is noted that the trailing edge separation in the post-stall part persists longer above the airfoil with increasing reduced frequency due to the increase in pressure adaptation lag, which delays the dynamic stall recovery. Furthermore, the dynamic stall C_N drop is decreased with increasing the reduced frequency. Notice the NFR decreases and the MDNS increases with increasing the reduced frequency. The same characteristics is visible for the X-FB-35-10 airfoil at $\alpha_m = STL\text{-}2°$ in forced transition flow.

At $\alpha_m = STL\text{-}2°$, the maximum overshoot of the dynamic C_N for the X-35-02 airfoil increases with increasing the reduced frequency. The pressure adaptation lag increases at high reduced frequencies, and the separation bubble above the airfoil develops less during the US-phase compared to lower reduced frequencies. As a result, the flow remains attached to higher angles of attack, leading to a higher C_N overshoot. The results show that the dynamic stall occurs before the (TSA) at low reduced frequencies, and the dynamic stall angle of attack moves towards the TSA with increasing reduced frequency. Notice that the normal force coefficient drops to the same order as the static curve after the dynamic stall at low reduced frequencies. However, with increasing reduced frequency, the normal coefficient drops less after the stall, which is related to the slower development of the trailing edge separation bubble above the airfoil due to the increased pressure lag. The NFR and MDNS increase with increasing reduced frequency. The same dynamic behavior is observed for the X-FB-35-10 airfoil at $\alpha_m = 10°$.

The dynamic stall characteristics of the X-35-02 airfoil in the post-stall region and free transition flow regime at a reduced frequency of $k = 0.032$ show that the normal force coefficient loops around the static curve. As the reduced frequency increases, the US-phase becomes more stable, and the cycles transform into a more oval shape, which is related to the increase in pressure lag. However, due to the large separation bubble above the airfoil in the post stall angle of attack, the size of the separation bubble starts to increase during the US-phase. Notice that these loops are clockwise. The point at which the separation bubble begins to expand can be detected as the maximum normal force coefficient in the US-phase. Note that this point moves to higher angles of attack with increasing reduced frequency. The reduced frequency does not affect the NFR; however, it only shifts slightly the phase of the extremum points. The MDNS decreases, with increasing the reduced frequency. Furthermore, the standard deviation of the normal coefficient in the loops decreases with increasing the reduced frequency. For the X-FB-35-10 airfoil the DS-phases closely follow the static curve due to a significant separation bubble in the post-stall region. An increase in reduced frequency slightly raises the NFR and MDNS, which is related to the not fully separated flow on the suction side of the airfoil at the beginning of the US-phase. Increasing the reduced frequency pulls this small, attached flow part above the airfoil to higher angles of attack.

The effect of the reduced frequency on the dynamic normal coefficient characteristics of both airfoils with VGs configuration in free and force transition flow regimes is presented in Fig. 13.

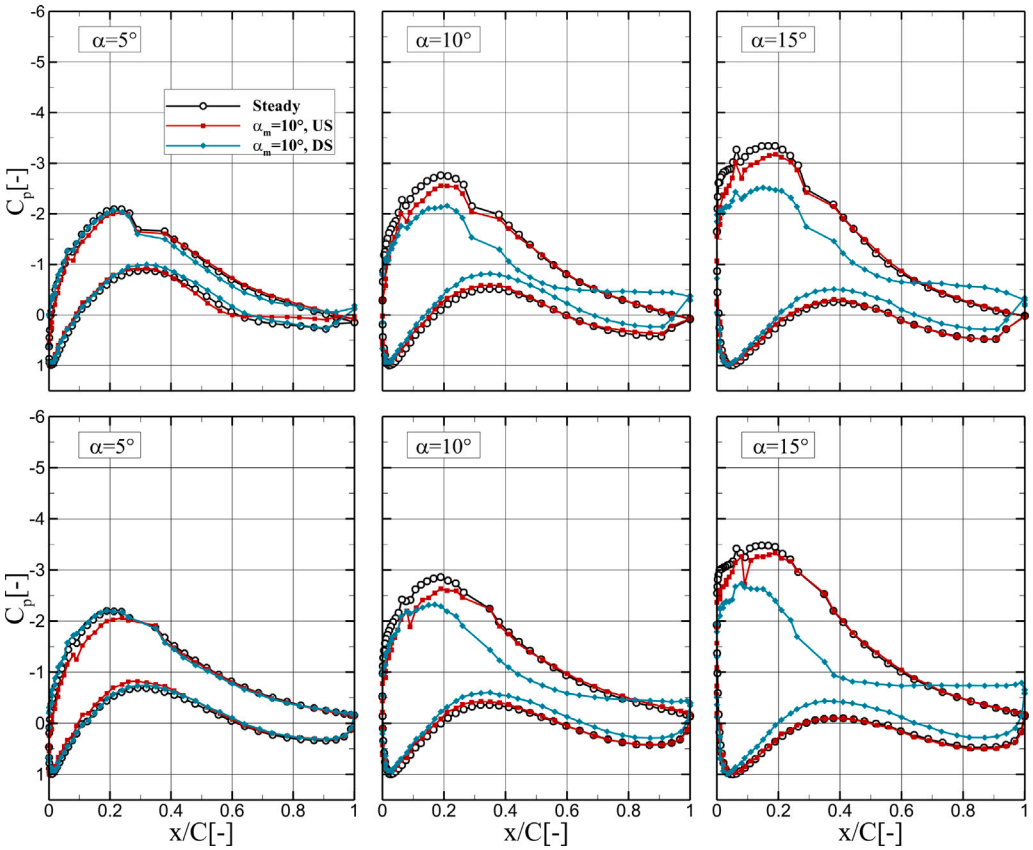

Fig. 10. Steady and dynamic Pressure coefficient distribution comparison in forced transition flow regime [$Re = 1 \times 10^6$, $k = 0.064$, $\alpha_m = 10°$, VG 0.3, Top: X-35-02, Bottom: X-FB-35-10].

The results for the X-35-02 airfoil with VGs located at 30% of the chord, at $\alpha_m = 10°$ and in free transition flow, show an increase in pressure lag with an increase in reduced frequency, while the TSA remains below the static stall angle of attack. This results in a reduction of C_N in the US-phase and an increase in C_N in the DS-phase. In contrast to the previous dynamic stall cases, the maximum overshoot occurs at a lower reduced frequency. Moreover, the trailing edge separation at the TSA remains longer above the airfoil surface than at lower reduced frequencies. The dynamic C_N at the BSA matches the static value only at a reduced frequency of k = 0.032, which increases with an increase in reduced frequency due to increased pressure lag. Note that the MDNS and NFR decrease as the reduced frequency increases.

Dynamic stall occurs when this airfoil's mean angle of attack is increased to $\alpha_m = STL\text{-}2°$. Due to a high TSA (30°) and a very high pressure gradient above the airfoil, along with a relatively low pressure adaptation lag, the most abrupt drop in C_N occurs at $k = 0.032$. In this case, the dynamic stall onset is below the TSA, and the dynamic C_N continues to fall well below the static post-stall C_N, which leads to a high NFR. Similar to the no-VGs case, the stall tends to be smoother with increasing reduced frequency. It is important to note that the maximum C_N overshoot occurs at $k = 0.064$, since the dynamic C_N slope in the US-phase decreases with increasing reduced frequency.

Dynamic stall is observed at all reduced frequencies for the flatback airfoil in forced transition flow with VGs configuration. Elevating the reduced frequency results in an increase in the dynamic stall angle of attack and the maximum dynamic C_N overshoot. Moreover, the recovery from dynamic stall is delayed as the reduced frequency increases. Additionally, bifurcation flow is evident during the DS-phase at reduced frequencies of $k = 0.064$ and $k = 0.096$. The NFR experiences a moderate reduction, while the MDNS increases with increasing the reduced frequency. With the slight increase of the mean angle of attack to $\alpha_m = STL\text{-}2°$, more abrupt dynamic stall is observed, and the bifurcation flow is eliminated. The dynamic stall characteristics of both airfoils with VGs in the post-stall range is very similar to those without VGs. These clockwise dynamic loops remain close to the static curve and a bifurcation flow condition is also visible for the flatback airfoil in the US-phase.

Fig. 14 shows the impact of VGs chord position on the dynamic normal coefficient characteristics of both airfoils in free and force transition flow regimes at $\alpha_m = 10°$ and $k = 0.062$. In free transition flow condition, both airfoils exhibit counter-clockwise dynamic loops in the attached flow region of the steady polars. The results indicate a slight increase in MDNS with VGs positioned closer to the trailing edge. This trend is also evident in the steady polars, where a higher normal coefficient slope is observed at the aft VGs chord position. However, this behavior is unexpected since forward-positioned VGs are known to stabilize the flow more effectively than aft-positioned VGs. This phenomenon may be related to the effect of VGs chord position on the indicial lift response of an airfoil and requires further investigation. It is noteworthy that the flatback airfoil exhibits a higher standard deviation of the normal coefficient at the DS-phase compared to the X-35-02 airfoil, and it is not affected by VGs chord position. In forced transition condition, the flow remains attached for VGs positioned at 20% of the chord. However, dynamic stall occurs for the cases with VGs positioned at 30% and 40% of the chord, and a high standard deviation of the normal force is visible in the DS-phase. Note that the flatback airfoil exhibits a smoother post-stall behavior than the X-35-02 airfoil.

4. Conclusions

The primary objective of this study is to investigate the impact of VGs on the dynamic stall characteristics of thick flatback and non-flatback wind turbine airfoils. The measurements were conducted in the LTT wind tunnel of the TU Delft. Two different airfoils, X-35-02

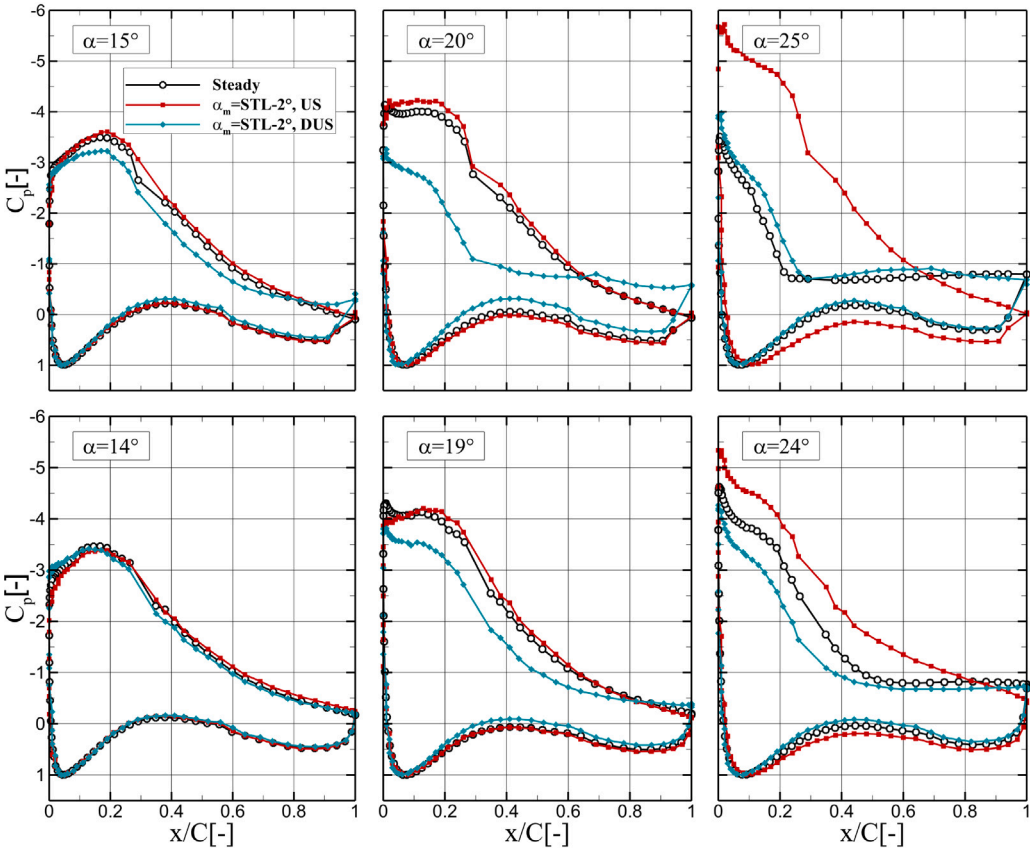

Fig. 11. Steady and dynamic Pressure coefficient distribution comparison in free transition flow regime [$Re = 1 \times 10^6$, $k = 0.064$, $\alpha_m = STL\text{-}2°$, VG 0.3, Top: X-35-02, Bottom: X-FB-35-10].

and X-FB-35-10, are tested at different mean angles of attack, reduced frequencies, VGs chord position, and in free and forced transition flow regimes. Aerodynamic coefficients were determined using surface pressure measurements.

The steady measurements indicate that the X-FB-35-10 airfoil exhibits a higher stall angle of attack, a higher maximum lift coefficient, and lower sensitivity to the leading edge roughness, compared to the X-35-02 airfoil. Increasing the thickness of the trailing edge reduces the pressure gradients above the airfoil, stabilizing the boundary layer and enhancing the airfoil's resistance to adverse pressure gradients. Additionally, installing VGs on the airfoil surface increases the maximum lift coefficient and stall angle of attack, while reducing the drag coefficient at high angles of attack and the sensitivity of the airfoil to leading edge roughness.

The dynamic measurements reveal that the X-FB-35-10 flatback airfoil exhibits more stable dynamic loops in the attached flow region of the lift curve, as evidenced by lower lift standard deviation, higher lift overshoot, and higher mean dynamic lift slope, owing to its superior suction side pressure gradient. In contrast, the X-35-02 airfoil exhibits less stable dynamic loops. The installation of VGs enhances flow stability during the US-phase, increases the C_N overshoot, and reduces the disparity between the dynamic loops of both airfoils.

In dynamic stall conditions, the trailing edge separation bubble, which develops over the airfoil during the US-phase, eventually leads to stall. For the flatback airfoil, this separation expansion is slower than for the sharp trailing edge airfoil, delaying the onset of dynamic stall and causing a higher C_N overshoot. Additionally, increasing the reduced frequency leads to a lag in pressure development on the airfoil's suction side, resulting in slower separation expansion and increased dynamic lift overshoot. Mounting VGs above the airfoil surface enhances flow stability during the US-phase and reduces the disparity between the dynamic cycles of both airfoils, resulting in a significant increase in maximum overshoot, particularly for the X-35-02 airfoil, compared to the no-VGs configuration. This increase in C_N overshoot leads to a greater C_N fall after a dynamic stall occurs. Increasing the reduced frequency results in a smoother C_N drop. Notably, if the expansion of the separation bubble above the airfoil is limited by increasing the reduced frequency, dynamic stall can be prevented.

In post-stall conditions, a large flow separation above the airfoil causes the dynamic lift to remain close to the static curve for both airfoils in the forced transition flow regime. Nevertheless, notable dynamic lift fluctuations are evident in the free transition flow condition, particularly in cases of smooth steady stall and when BSA approaches the steady stall angle of attack.

The chord position of the VGs has a minor impact on the dynamic normal coefficient cycles in the attached flow condition. However, VGs can be utilized to delay the onset of dynamic stall if the TSA is beyond the steady stall angle of attack.

This research demonstrates that using VGs can enhance flow stability during the US-phase for both airfoils, with a more pronounced effect observed for the non-flatback airfoil. Increasing the trailing edge thickness, installing VGs above the airfoil, and increasing the reduced frequency can delay the onset of the dynamic stall and increase the C_N overshoot. These modifications can have a significant impact on turbine operation. Furthermore, it is observed that the VGs and high reduced frequencies, reduces the fall of the C_N, if a dynamic stall occurs. Dynamic stall prevention can avoid vortex-induced vibrations of the rotor blade during high turbulence conditions, ultimately reducing the induced vibrations loads, improving overall efficiency, lifetime, and reliability of the turbine, and reducing sensitivity to wind fluctuations. However, this approach can lead to very high C_N overshoots, potentially overstressing turbine components, particularly in combination with flatback airfoils. Further research is necessary to fully understand the potential of VGs and flatback airfoils for improving the dynamic induced vibration loads of rotor blades.

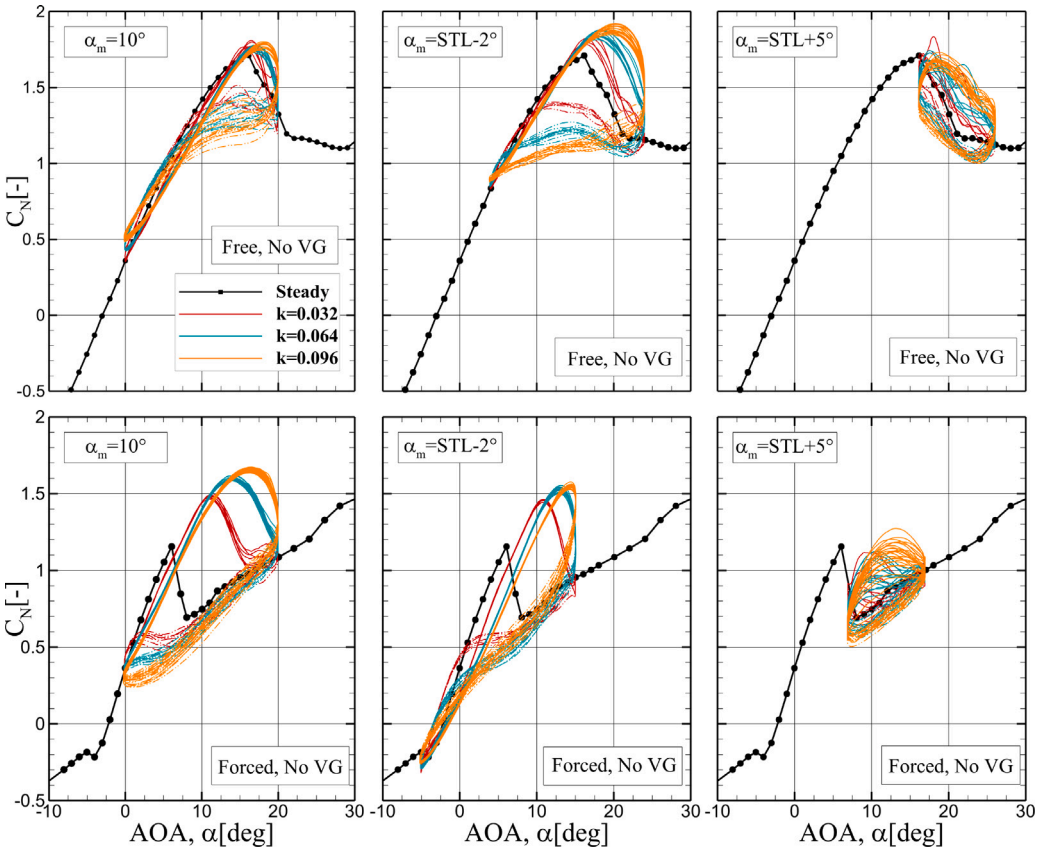

Fig. 12. Effect of the reduced frequency on the normal coefficient in free and forced transition flow regimes [$Re = 1 \times 10^6$, Top: X-35-02, Bottom: X-FB-35-10].

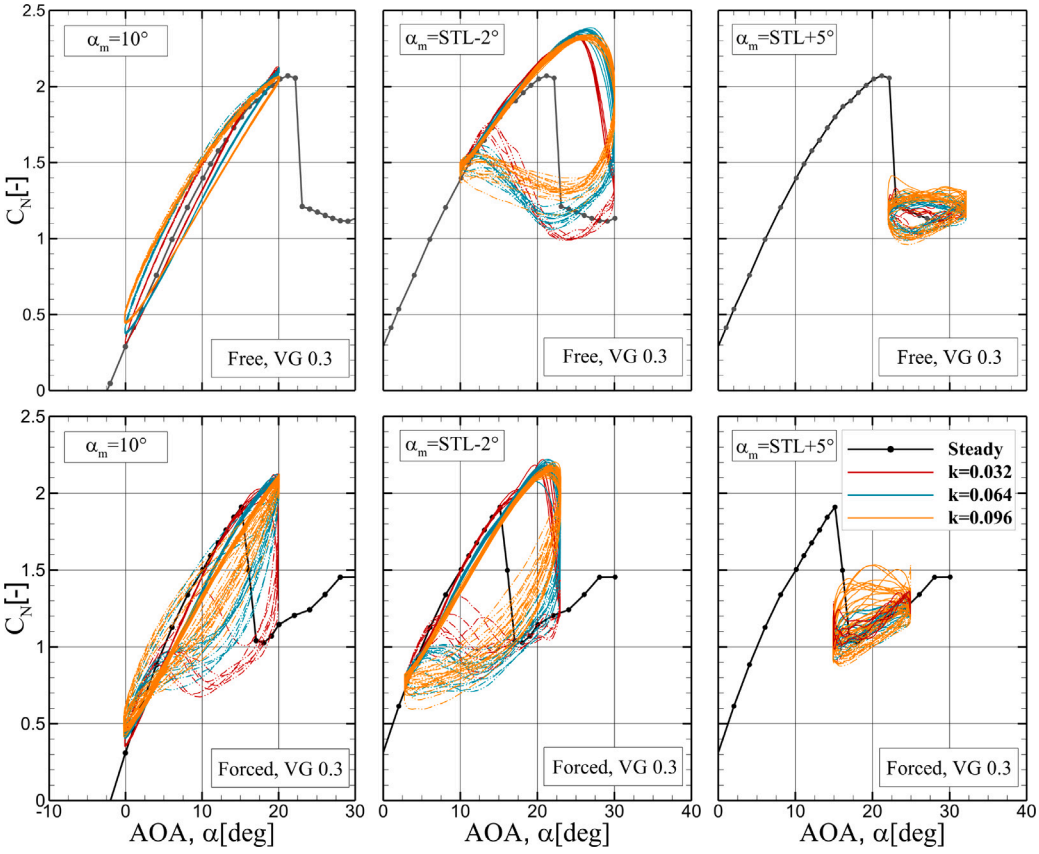

Fig. 13. Effect of the reduced frequency on the normal coefficient in free and forced transition flow regimes [$Re = 1 \times 10^6$, VG 0.3, Top: X-35-02, Bottom: X-FB-35-10].

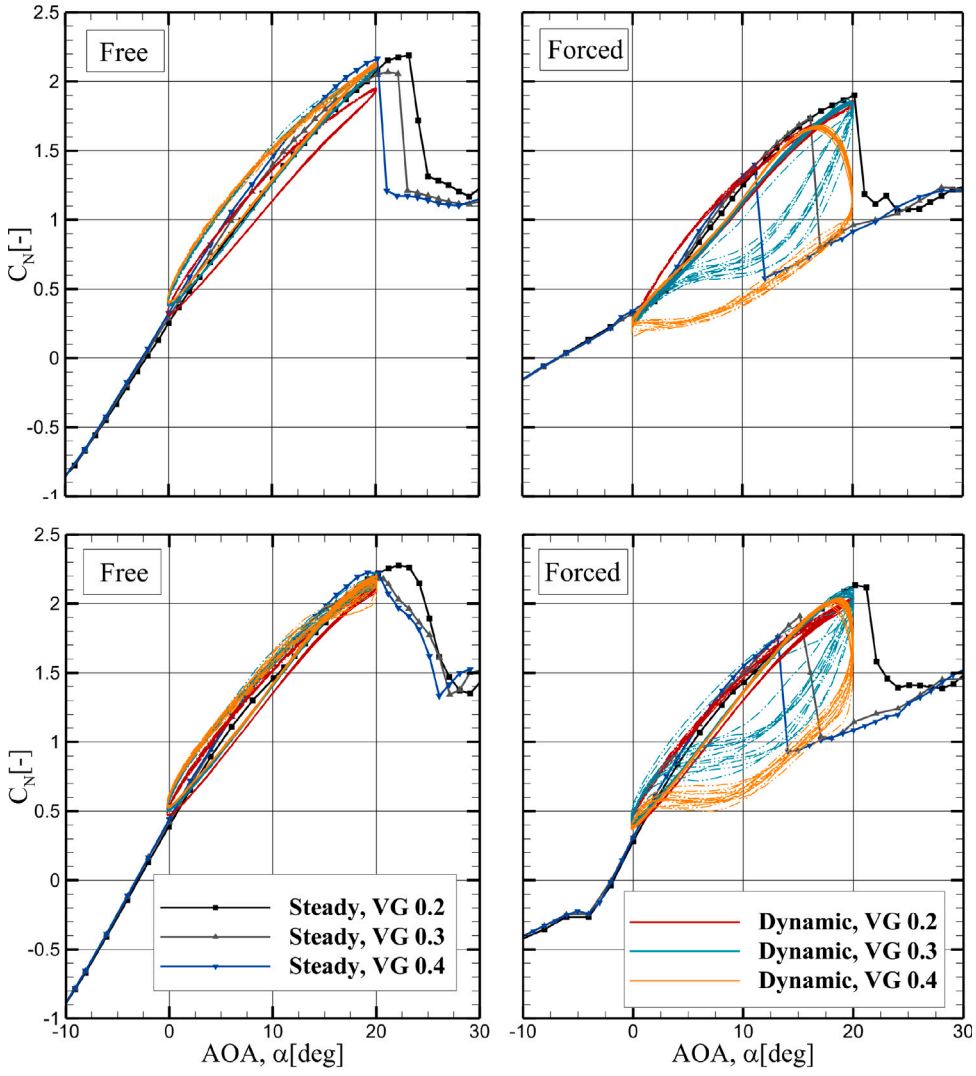

Fig. 14. Effect of the VGs chord position on the normal coefficient in free and forced transition flow regimes [$Re = 1 \times 10^6$, $k = 0.064$, $\alpha_m = 10°$, Top: X-35-02, Bottom: X-FB-35-10].

CRediT authorship contribution statement

Mehdi Doosttalab: Writing – review & editing, Writing – original draft, Visualization, Validation, Software, Methodology, Investigation, Formal analysis, Data curation. **Carlos Simao Ferreira:** Supervision. **Daniele Ragni:** Supervision. **Wei Yu:** Supervision. **Christof Rautmann:** Resources, Funding acquisition.

Declaration of competing interest

The authors declare the following financial interests/personal relationships which may be considered as potential competing interests: Mehdi Doosttalab reports financial support was provided by Nordex Energy GmbH. Mehdi Doosttalab reports a relationship with Nordex Energy GmbH that includes: employment. If there are other authors, they declare that they have no known competing financial interests or personal relationships that could have appeared to influence the work reported in this paper.

Acknowledgments

This work was funded by Nordex Energy SE & Co. KG, Germany and the authors are very grateful for this support.

Appendix

Bergh and Tijdeman [40] concluded that varying the frequency of constant fluctuations for a given pressure measurement system with a constant pressure input results in the system's frequency response. Having the frequency response of a system makes it possible to calculate the system's time response to any random input signal. This theory decomposes a pressure measurement system into an N subsection, in which the input pressure of a section is the output pressure of the N-1 section. The pressure transfer function for a single pressure measurement system i.e., for every subsystem, is given by:

$$\frac{p_1}{p_0} = \left[cosh\langle \varphi L \rangle + \frac{V_v}{V_t} \left(\sigma + \frac{1}{k} \right) n\varphi L sinh\langle \varphi L \rangle \right]^{-1} \tag{1}$$

$$\varphi = \frac{\nu}{\alpha_0} \sqrt{\frac{J_0 \langle \alpha \rangle}{J_2 \langle \alpha \rangle}} \sqrt{\frac{\gamma}{n}} \tag{2}$$

$$\alpha = i\sqrt{iR} \sqrt{\frac{\rho_s v}{\mu}} \tag{3}$$

$$n = \left(1 + \frac{\gamma - 1}{\gamma} \frac{J_2 \left\langle \alpha \sqrt{P_r} \right\rangle}{J_0 \left\langle \alpha \sqrt{P_r} \right\rangle} \right)^{-1} \tag{4}$$

Here V_v is the pressure transducer volume, V_t is the tube volume, R is the tube radius, L is the length of the tube, i is the imaginary number,

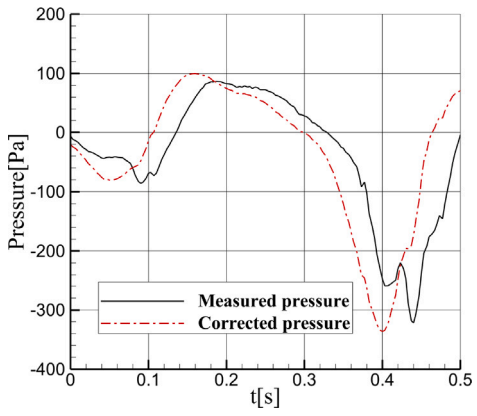

Fig. A.15. Comparison between the measured and the corrected data of a pressure tap of X-35-02 airfoil [$Re = 1 \times 10^6$].

J_n is the Bessel function of the first kind of order n, k is the polytropic constant for the volumes, α_0 is the speed of sound. ρ_s is the mean density, α is the shear wave number, μ is the absolute fluid viscosity, γ is the specific heat ratio, ν is the frequency. υ is the pressure transducer volume, P_r is the Prandtl number. σ is the dimensionless volume increase in the pressure transducer due to diaphragm deflection. For several pressure tubes, which are connected in series:

$$\frac{p_N}{p_0} = \frac{p_N}{p_{N-1}} \dots \frac{p_1}{p_0} \tag{5}$$

Defining the relation between each subsystem, a square step response along with Fast Fourier Transformation (FFT) and inverse FFT are used to predict the domain frequency response of the system [38]. Fig. A.15 shows the difference between the measured uncorrected pressure and corrected pressure for the phase delay and amplitude on one pressure tap near the trailing edge at the suction side of the X-35-02 airfoil. Since the connection characteristics, including tube length, cavities, and potential adaptors between the pressure sensors and the pressure coupling connection within the pressure acquisition system, are unknown, a CFD simulation at 1 Hz was utilized in the linear region of the lift polar to determine the equivalent tube length and diameter of the unidentified components, ultimately validating the pressure correction method.

Appendix B. Nomenclature

B.1. Greek letters

α = angle of attack [°]
α_0 = speed of sound [m/s]
α_j = shear wave number [–]
α_m = mean angle of attack [°]
γ = specific heat ratio [–]
μ = absolute viscosity [Ns/m^2]
ν = frequency [Hz]
ω = angular frequency [rad/s]
ρ_s = mean density [kg/m^3]
σ = diaphragm volume increase [–]

B.2. Symbols

A = amplitude of oscillation [°]
C = chord [m]
C_L = lift coefficient [–]
C_D = drag coefficient [–]
C_M = moment coefficient [–]
C_N = normal coefficient [–]
C_p = pressure coefficient [–]
i = imaginary number [–]
J_n = Bessel function [–]
k = reduced frequency [–]
k_p = polytropic constant [–]
L = tube length [m]
P_r = Prandtl number [–]
R= tube radius [m]
Re = Reynolds number [–]
R_{kk} = roughness Reynolds number [–]
t = time [s]
υ = pressure transducer volume [m^3]
V = airfoil relative velocity [m/s]
V_{in} = Cut in velocity [m/s]
V_{out} = Cut out velocity [m/s]
V_r = Rated velocity [m/s]
V_t = tube volume [m^3]
V_υ = pressure transducer volume [m^3]

B.3. Abbreviations

AOA = Angle Of Attack [°]
BSA = Bottom Stagnation Angle [°]
CFD = Computational Fluid Dynamics
DS = Down-Stroke
ETM = Extreme Turbulence Model
FFT = Fast Fourier Transformation
$LEVoGs$ = Leading Edge Vortex Generators
$MDNS$ = Mean Dynamic Normal Slope [Rad]
NFR = Normal Force Range [–], the distance between maximum and minimum C_N
$NREL$=National Renewable Energy Laboratory
NTM = Normal Turbulence Model
$PISO$ = Pressure Implicit Splitting of Operators
PIV = Particle Image Velocimetry
SST = Shear Stress Transport
STL = Stall
TSA = Top Stagnation Angle [°]
$URANS$ = Unsteady Reynolds-Averaged Navier–Stokes
US = Up-Stroke
VGs = Vortex Generators

References

[1] María Isabel Blanco, The economics of wind energy, Renew. Sustain. Energy Rev. 13 (6–7) (2009) 1372–1382, http://dx.doi.org/10.1016/j.rser.2008.09.004.
[2] Thomas D. Ashwill, Parametric Study for Large Wind Turbine Blades: WindPACT Blade System Design Studies, Technical Report, Sandia National Lab. (SNL-NM), Albuquerque, NM (United States); Sandia ..., 2002, http://dx.doi.org/10.2172/801402.
[3] Lin Wang, Xiongwei Liu, Athanasios Kolios, State of the art in the aeroelasticity of wind turbine blades: Aeroelastic modelling, Renew. Sustain. Energy Rev. 64 (2016) 195–210, http://dx.doi.org/10.1016/j.rser.2016.06.007.
[4] J. Gordon Leishman, Challenges in modelling the unsteady aerodynamics of wind turbines, Wind. Energy An Int. J. Prog. Appl. Wind. Power Convers. Technol. 5 (2–3) (2002) 85–132, http://dx.doi.org/10.1002/we.62.
[5] Gordon J. Leishman, Principles of Helicopter Aerodynamics with CD Extra, Cambridge university press, ISBN: 0521858607, 2006.
[6] Ricardo Pereira, Gerard Schepers, Marilena D. Pavel, Validation of the Beddoes–Leishman dynamic stall model for horizontal axis wind turbines using MEXICO data, Wind. Energy 16 (2) (2013) 207–219, http://dx.doi.org/10.1002/we.541.
[7] Max Kramer, Increase in the Maximum Lift of an Airplane Wing Due to a Sudden Increase in Its Effective Angle of Attack Resulting from a Gust, Technical Report, 1932.
[8] L.E. Ericsson, Comments on unsteady airfoil stall, J. Aircr. 4 (5) (1967) 478–480.
[9] Franklin O. Carta, Effect of unsteady pressure gradient reduction on dynamic stall delay, J. Aircr. 8 (10) (1971) 839–841.
[10] Wayne Johnson, Norman D. Ham, On the mechanism of dynamic stall, J. Am. Helicopter Soc. 17 (4) (1972) 36–45.

[11] Lars E. Ericsson, J. Peter Reding, Dynamic stall of helicopter blades, J. Am. Helicopter Soc. 17 (1) (1972) 11–19.
[12] W.J. McCroskey, Inviscid flowfield of an unsteady airfoil, AIAA J. 11 (8) (1973) 1130–1137, http://dx.doi.org/10.2514/6.1972-681.
[13] T.S. Beddoes, Representation of airfoil behaviour, Vertica 7 (2) (1983).
[14] Kenneth W. McAlister, Lawrence W. Carr, Water tunnel visualizations of dynamic stall, 1979.
[15] R. Scruggs, J. Nash, R. Singleton, Analysis of flow-reversal delay for a pitching airfoil, in: 12th Aerospace Sciences Meeting, 1974, p. 183, http://dx.doi.org/10.2514/6.1974-183.
[16] Demetri P. Telionis, Calculations of time-dependent boundary layers, Unsteady Aerodyn. 1 (1975) 155–190.
[17] W.J. MdcCroskey, Some current research in unsteady fluid dynamics-the 1976 freeman scholar lecture, J. Fluids Eng. (1977) 8–39.
[18] Norman D. Ham, Aerodynamic loading on a two-dimensional airfoil during dynamic stall, AIAA J. 6 (10) (1968) 1927–1934, http://dx.doi.org/10.2514/3.4902.
[19] W.J. McCroskey, Recent Developments in Rotor Blade Stall, in: AGARD CP, vol. 111, 1972.
[20] T.S. Beddoes, A qualitative discussion of dynamic stall, in: AGARD Special Course on Unsteady Aerodynamics, AGARD Report, 679, 1979.
[21] T.S. Beddoes, Onset of leading edge separation effects under dynamic conditions and low mach number, in: American Helicopter Society, Annual National Forum, 34 Th, Washington, D. C, Proceedings, Research Supported By the Ministry of Defence,(Procurement Executive), vol. 15, (17) 1978.
[22] PETER LORBER, Compressibility effects on the dynamic stall of a three-dimensional wing, in: 30th Aerospace Sciences Meeting and Exhibit, 1992, p. 191, http://dx.doi.org/10.2514/6.1992-191.
[23] M.S. Chandrasekhara, L. W Carr, Compressibility Effects on Dynamic Stall of Oscillation Airfoil, in: AGARD, 1994, CP-552.
[24] J. Liiva, F.J. Davenport, L. Gray, I.C. Walton, 2-D tests of airfoils oscillating near stall, in: USAAVLABS, (TR 68-13, Vols. I II), 1968.
[25] Mrs. M.E. Wood, Results of Oscillatory Pitch and Ramp Tests on the NACA 0012 Blade Section, Aircraft Research Association Limited, 1979.
[26] D. De Tavernier, Carlos Ferreira, A. Viré, B LeBlanc, S Bernardy, Controlling dynamic stall using vortex generators on a wind turbine airfoil, Renew. Energy 172 (2021) 1194–1211, http://dx.doi.org/10.1016/j.renene.2021.03.019.
[27] Holger Mai, Guido Dietz, Wolfgang Geißler, Kai Richter, Johannes Bosbach, Hugues Richard, Klaus de Groot, Dynamic stall control by leading edge vortex generators, J. Am. Helicopter Soc. 53 (1) (2008) 26–36, http://dx.doi.org/10.4050/JAHS.53.26.
[28] Benjamin Heine, Karen Mulleners, Gilles Joubert, Markus Raffel, Dynamic stall control by passive disturbance generators, AIAA J. 51 (9) (2013) 2086–2097, http://dx.doi.org/10.2514/1.J051525.
[29] Arnaud Le Pape, Michael Costes, Francois Richez, Gilles Joubert, F David, J-M Deluc, Dynamic stall control using deployable leading-edge vortex generators, AIAA J. 50 (10) (2012) 2135–2145, http://dx.doi.org/10.2514/1.J051452.
[30] Morten Hartvig Hansen, Mac Gaunaa, Helge Aagaard Madsen, A Beddoes-Leishman type dynamic stall model in state-space and indicial formulations, ISBN: 87-550-3090-4, 2004.
[31] T.S. Beddoes, A synthesis of unsteady aerodynamic effects including stall hysteresis, Vertica 1 (2) (1976) 113–123.
[32] R.B. Green, R.A. McD Galbraith, Dynamic recovery to fully attached aerofoil flow from deep stall, AIAA J. 33 (8) (1995) 1433–1440, http://dx.doi.org/10.2514/3.12565.
[33] Dale Berg, Jose Zayas, Aerodynamic and aeroacoustic properties of flatback airfoils, in: 46th AIAA Aerospace Sciences Meeting and Exhibit, 2008, p. 1455, http://dx.doi.org/10.2514/6.2008-1455.
[34] K.J. Standish, C.P. Van Dam, Aerodynamic analysis of blunt trailing edge airfoils, J. Sol. Energy Eng. 125 (4) (2003) 479–487, http://dx.doi.org/10.1115/1.1629103.
[35] Galen Brandt Schubauer, W.G. Spangenberg, Forced mixing in boundary layers, J. Fluid Mech. 8 (1) (1960) 10–32, http://dx.doi.org/10.1017/S0022112060000372.
[36] W.A. Timmer, RPJOM Van Rooij, Summary of the delft university wind turbine dedicated airfoils, J. Sol. Energy Eng. 125 (4) (2003) 488–496, http://dx.doi.org/10.1115/1.1626129.
[37] Delft University of Technology. Low turbulence tunnel (LTT), 2024, URL https://www.tudelft.nl/lr/organisatie/afdelingen/flow-physics-and-technology/facilities/low-speed-wind-tunnels/low-turbulence-tunnel. (Accessed 16 January 2024).
[38] Biao Lu, Michael Bragg, Experimental investigation of the wake-survey method for a bluff body with a highly turbulent wake, in: 20th AIAA Applied Aerodynamics Conference, 2002, p. 3060, http://dx.doi.org/10.2514/6.2002-3060.
[39] C. Dalton, Allen and Vincenti blockage corrections in a wind tunnel, AIAA J. 9 (9) (1971) 1864–1865, http://dx.doi.org/10.2514/3.6435.
[40] H. Bergh, Hendrik Tijdeman, Theoretical and Experimental Results for the Dynamic Response of Pressure Measuring Systems, National Aero and astronautical research institute Amsterdam, 1965.
[41] Daniel Baldacchino, Carlos Ferreira, Delphine De Tavernier, WA Timmer, GJW Van Bussel, Experimental parameter study for passive vortex generators on a 30% thick airfoil, Wind. Energy 21 (9) (2018) 745–765, http://dx.doi.org/10.1002/we.2191.